COMMUNICATION

Communication

W.-Z. Han,* M.-S. Ding, R. L. Narayana, Z.-W. Shan 1700357

In Situ Study of Deformation Twinning and Detwinning in Helium Irradiated Small-Volume Copper

In situ nanomechanical tests performed inside a transmission electron microscope reveals that twinning and detwinning occurs readily in helium irradiated copper under both tension and compression. Continuous shearing of helium bubbles by Shockley partials leads to twin formation whereas the residual back-stress accumulated from dislocation-bubble interactions assist in detwinning.

ADVANCED ENGINEERING MATERIALS
www.aem-journal.com

In Situ Study of Deformation Twinning and Detwinning in Helium Irradiated Small-Volume Copper

Q1 Wei-Zhong Han,* Ming-Shuai Ding, R. Lakshmi Narayana, and Zhi-Wei Shan Q2

The influence of nanoscale helium bubbles on the deformation twinning and detwinning behavior of submicron-sized Cu is investigated under tension, compression, and cyclic loading. In situ nanomechanical tests performed inside a transmission electron microscope reveals that twinning and detwinning occurs readily in helium irradiated copper under both tension and compression. Continuous shearing of helium bubbles by Shockley partials leads to twin formation, whereas the residual back-stress accumulated from dislocation-bubble interactions assist in detwinning. These interactions also elevate the critical shear stress for partial dislocation slip in helium irradiated Cu compared to that in fully dense Cu. The growth twin boundary can significantly enhance the twinning stress in helium irradiated Cu pillar, and deformation twin-growth twin boundary interaction promotes the formation of internal crack and thus accelerates failure. The effect of crystallographic orientation and sample size on the overall deformation characteristics of helium irradiated Cu is briefly discussed. The current studies show that deformation twinning and detwinning are also active deformation models in helium irradiated small-volume copper.

In nuclear reactor environments, helium ions are generated from (n,α) Q3 reactions that occur during high intensity of neutron Q4 irradiation.[1,2] Being an insoluble element, when helium ions come in contact with metals, it preferentially combines with vacancies and precipitates out as gas bubbles.[3–10] Furthermore, it agglomerates along microstructural sinks such as dislocations, precipitates, or interfaces, resulting in swelling, blistering, and high temperature embrittlement of the reactor components.[11–16] Since the production of helium atoms is unavoidable in a nuclear reactor, the adverse effects of helium on the mechanical properties of reactor materials have to be accommodated or eliminated during design. For this purpose, the influence of helium production on microstructural evolution and deformation mechanisms needs to be understood in detail.

In the quest to manage the deleterious effects of helium bubbles, lots of studies were dedicated toward tuning their size and distribution by engineering well defined sinks such as dislocations, precipitates, grain boundaries, and interfaces.[16–20] Experimental investigations indicated that such engineered sinks can effectively suppress the detrimental effects of helium bubbles.[21–30] Therefore, nanolaminates, nanograined metals, and oxide dispersion-strengthened alloys, which meet these specific microstructural requirements were proposed as potential replacements for existing reactor materials.[21–30]

Recent studies indicated that the effect of radiation helium bubbles on the mechanical properties of metals and alloys is sensitive to length scale. For example, in bulk metals, helium bubbles accumulate along sinks, such as grain boundaries, and cause macroscopic embrittlement at elevated temperature.[11–16] In contrast, nanoscale helium bubbles enhance the yield strength and deformability of submicron-sized single crystalline metals.[31–37] This is because nanoscale helium bubbles not only behave as shearable dislocation obstructers, but also double up as active internal dislocation sources.[36] Therefore, although nanoscale bubbles partially impede the motion of full dislocations, they also promote dislocation nucleation and dislocation-dislocation interactions, hence stabilizing the stress–strain response of the small-volume metals.[36] Apart from dislocation slip, submicron-sized metallic specimens also show a tendency to accommodate plastic deformation by twinning.[38–47] While twinning and its interactions with dislocations and grain boundaries has been studied extensively in pristine, non-irradiated materials, its behavior in the presence of irradiation induced nanoscale helium bubbles has not yet been explored in detail.

In this study, we performed in situ mechanical tests on helium implanted small-volume copper, inside a transmission electron microscope (TEM), and explored its deformation behavior while varying the loading geometry and sample orientation. Copper was chosen as a model material because it has a moderately stacking fault energy of $\approx$40 mJ m^{-2}.[44] Low stacking fault energy promotes twinning in submicron-sized pillars and offers additional avenues for investigating the interactions between different defects.[46] From our study, it was

Dr. W.-Z. Han, Dr. M.-S. Ding, Dr. R. L. Narayana, Dr. Z.-W. Shan
Center for Advancing Materials Performance from the Nanoscale (CAMP-Nano) & Hysitron Applied Research Center in China (HARCC), State Key Laboratory for Mechanical Behavior of Materials, Xi'an Jiaotong University, Xi'an 710049, China
E-mail: wzhanxjtu@mail.xjtu.edu.cn; wzhanmail@gmail.com

Dr. R. L. Narayana
Department of Materials Science and Engineering, Carnegie Mellon University, Pittsburgh, PA 15213, USA

DOI: 10.1002/adem.201700357

revealed that twinning and detwinning play a key role in the plastic deformation of helium irradiated submicron-sized Cu pillars.

2. Results and Discussion

2.1. Twinning in [$1\bar{1}\bar{3}$] Helium Irradiated Cu Single Crystal under In Situ Compression

TEM images taken at various stages of compression on a rectangular helium nano bubbled Cu (NB–Cu) single crystal pillar with width of ≈95 nm, loaded along its [$1\bar{1}\bar{3}$] direction, are shown in **Figure 1**. As can be seen in Figure 1a, the NB–Cu pillar, prior to loading, has a high density of helium bubbles distributed homogeneously across the whole sample. Inset in the figure[Q5] displays the selected area electron diffraction (SAED) pattern of the region marked by the black circle in Figure 1a. From this pattern, it was determined that the electron beam is roughly parallel to the [110] direction of the NB–Cu single crystal, which is also the correct orientation for observing deformation twinning in face-centered cubic metals. Upon loading this pillar, no discernable changes can be observed on the sample up to a strain of ≈6% although the sample yield at a strain of ≈3% with a yield strength of ≈1 GPa. However, once beyond 6% engineering strain, three very thin, dark lines appear at the two extremities of the pillar, and are marked with black arrows in Figure 1b (for real-time viewing, see movie S1 in Supplementary Information (SI)). Amongst the two lines formed near the loading end of the pillar, the one situated closer to the diamond punch is narrow and corresponds to a stacking fault, whereas the one lying above it, is much thicker and resembles a microtwin. Alternatively, the dark thin line formed at the other end of the pillar corresponds to a stacking fault. The observation of stacking faults in the pillar suggests that Shockley partial dislocations can easily penetrate the high density of helium bubbles in NB–Cu. In fact, continuous slip of these Shockley partials are responsible for the formation of a microtwin. With further compressive loading, the microtwin starts to thicken and reaches a width of ≈10 nm, as shown in Figure 1c. Following this, the twin boundaries propagate outward and at a peak load of 1.3 GPa, the thickness of twin was found to be ≈38 nm, as indicated in Figure 1d. It is noteworthy that the surface of the NB–Cu pillar has a zigzag appearance due to the occurrence of deformation twinning. In contrast, owing to full dislocation slip, the surfaces of fully dense Cu (FD–Cu) pillars and NB–Cu pillars contain sharp slip steps and a curved smooth surface, respectively.[36]

During unloading, the diamond punch adheres to the NB–Cu pillar and introduces a tensile load of ≈300 MPa, which appears as a negative overshoot in the unloading segment of the stress–strain curve displayed in Figure 1g. As seen from the movie S1, this small tensile stress is sufficient to nucleate a small internal twin or secondary twin while also triggering the partial detwinning of the previously formed primary twin (the primary twin thickness was reduced obviously when comparing Figure 1d,e). These features have been specifically highlighted in Figure 1e and f. The inset in Figure 1e, which contains the

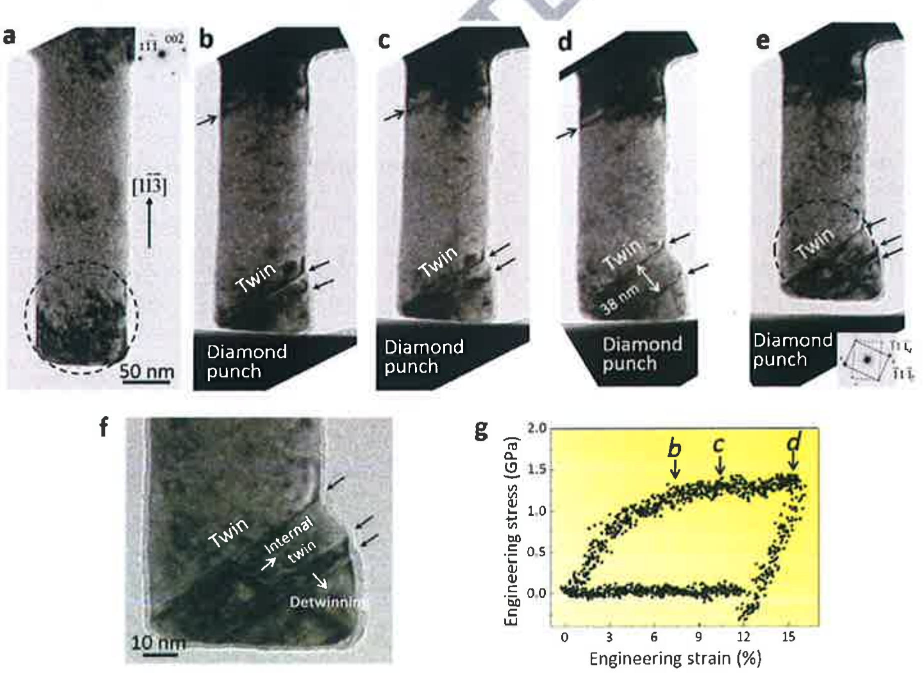

Figure 1. In situ compression test of helium irradiated Cu, loaded along [$1\bar{1}\bar{3}$]. (a) TEM image of a rectangular helium irradiated Cu sample used for in situ compression; (b) Deformation twins nucleate near the extremities of the pillar, once strain >6%; (c) twin thickens with further compression; (d) A zigzag surface feature is formed after twinning; (e) A Small internal twin is formed, and partial de-twinning of the primary twin occurs during unloading and subsequent load reversal; (f) Magnified image showing the newly formed internal twin and occurrence of partial de-twinning; (g) engineering stress–strain curve of the compression test (points marked on the curve with black arrows correspond to the image labels b–d).

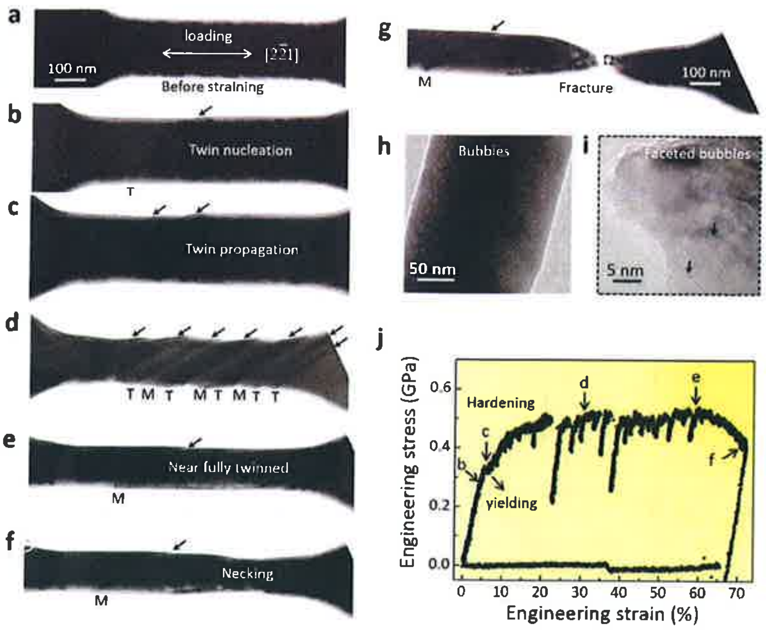

Figure 2. In situ tensile test of helium irradiated Cu, loaded along [2$\bar{2}$1]. (a) TEM image of a single crystalline dog-bone helium irradiated Cu sample used for the in situ tensile study; (b) A twin embryo nucleates, creating a surface offset on the upper edge of the specimen; (c) Multiple deformation twins nucleate with increasing tensile strain; (d) alternating layers of twins (*T*) and matrix (*M*) imparts a zigzag appearance on both edges of the specimen (e) Twins propagate throughout the sample with increasing strain; (f) Dislocation slip initiates after complete twinning (one matrix colony remains) and sample necks; (g) sample necks down to a point before fracture; (h) Magnified image highlighting nanoscale helium bubbles in the fractured sample; (i) Local high resolution image reveals faceting of bubbles and existence of stacking fault debris; (j) Engineering stress strain curve of the tensile test (points marked on the curve with black arrows correspond to the image labels b–f).

SAED pattern of the region marked in the figure, indicates the twin-matrix orientation relationship. The internal twin or secondary twin, formed inside the primary thick deformation twin, is oriented at an angle of 70.5°, with respect to the primary twinning plane. It is also observed that partial detwinning only occurs in the lower part of the primary twin, but also facilitates its shrinkage (see Figure 1f).

By synchronously observing the evolution of engineering stress and strain with the recording of movie S1, all critical events mentioned in the preceding discussion have been marked on the engineering stress–strain curve shown in Figure 1g. In the entire loading process, the engineering stress–strain curve remains free from sudden strain jumps that usually accompany twin nucleation. The steady response of the stress–strain curve in this test likely due to the strong obstructive effect of helium bubbles and the complex state of stress imposed on it during compression.[36] Also, from this figure, it was revealed that the primary deformation twin forms at a stress level of ≈1.25 GPa, which further corresponds to a critical resolved shear stress (CRSS) of 0.5 GPa. However, as noted before, internal deformation twinning and partial detwinning of the primary twin occurs at a much lower stress level (≈300 MPa), which is comparable to the detwinning induced by the migration of incoherent twin boundary in a nanotwinned copper.[48] This implies that the back stress developed from dislocation-bubble interactions during compression was sufficient to assist detwinning and internal twinning during unloading.

2.2. Twinning in Helium Irradiated Cu Single Crystal under In Situ Tension

The NB–Cu tensile sample, as shown in **Figure 2**a, has an initial width of ≈205 nm and was loaded along its [2$\bar{2}$1] direction. On loading the sample, a deformation twin embryo nucleates just before the onset of yielding and is marked with a black arrow in Figure 2b (also see movie S2). This twin embryo nucleates at a stress of 0.3 GPa, which corresponds to a CRSS of 0.14 GPa (marked with a black arrow in the engineering stress–strain curve shown in Figure 2j). Also, while the upper surface of the sample develops a tiny offset when the twin embryo forms, the lower surface remains smooth (see Figure 2b). Since the deformation twin embryo front has not propagated to the other edge of the specimen, the stress–strain response shown in Figure 2j remains linear elastic, even beyond the twin embryo nucleation point. Once the deformation twin embryo penetrates the entire pillar, as seen in Figure 2c, the stress-strain curve also registers a yield event (see the tiny strain jump at yielding in Figure 2j). Further straining promotes the formation of multiple deformation twins, all of which contribute to the zigzag appearance of the NB–Cu pillar surfaces, as seen in Figure 2d. These alternating layers of the twin (marked as *T*) and the untwinned part (marked as *M*) resemble a multilayered structure with twin boundaries as interfaces. In Figure 2j, between points c and d marked on the engineering stress–strain curve, the stress continuously increases from ≈0.35 to 0.5 GPa, implying that the sample undergoes significant strain hardening within this range. It is likely that the observed hardening behavior is a consequence of the continuous activation of twins, whose sources require a higher critical stress to operate. Unlike single source dislocation slip, where the source can keep operating at a constant stress level, and produce a large slip step on the slip plane, the twinning process induces a zigzag morphology across the specimen. Besides, after twins nucleate in the specimen, the numerous interfaces, in the form of twin boundaries can further enhance strain hardening by blocking dislocation slip.[49–53]

When the strain increases further, the NB–Cu pillar continues deforming via twinning and finally evolves into a fully twinned sample with a new twin orientation, barring one remaining tiny matrix colony marked in Figure 2e. This tiny matrix colony might have survived twinning when slipping Shockley partials, which initiated twinning, were locally obstructed by the helium bubbles and dislocation debris. Up until this point, each abrupt stress drop in the stress–strain curve roughly corresponds to a twinning event in the sample. Beyond this strain level, the

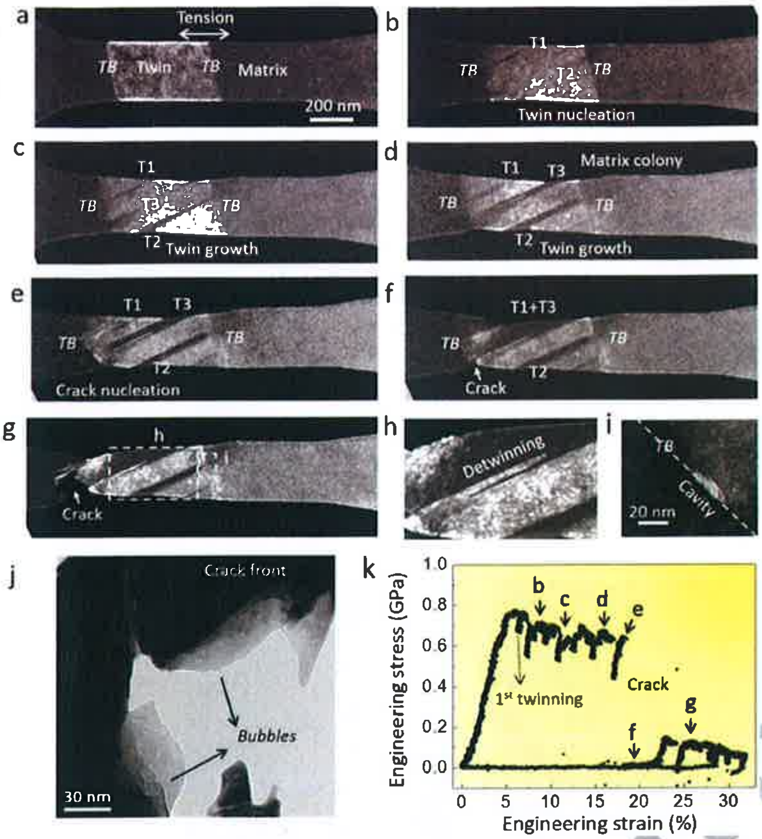

Figure 3. In situ tensile deformation of a growth twin embedded helium irradiated Cu sample. (a) Dark field TEM image showing the growth twin in the tensile sample; (b) Secondary twins nucleate inside the growth twin on loading; (c) More deformation twins nucleate from the sample edges in the growth twin, with straining; (d) Deformation twins interact with the boundaries of growth twin; (e) stress concentration develops at the deformation twin-growth twin boundary interface. (f) Crack nucleates from the stress concentration. (g) Partial detwinning of deformation twin occurs due to crack formation induced strain relaxation; (h) Magnified image of partially detwinned region in (g); (i) Magnified image of a cavity nucleated at the growth twin boundary-deformation twin interface, on unloading; (j) Enlarged helium bubbles seen at the fracture surface, indicating their coalescence; (k) Engineering stress strain curve of the tensile test (points marked on the curve with black arrows correspond to the image labels b–g).

sample deforms via full dislocation slip, and undergoes near uniform elongation followed by local necking, as shown in Figure 2f. During this stage, the stress strain curve is smooth, but shows a gradual drop in slope with increasing strain. However, the observed strain softening is merely a consequence of the reduction in cross section area of the sample after large strains. Since the sample is much thinner and narrower than what it was before loading, it is now only capable of supporting lower loads while undergoing deformation via full dislocation slip.

Final fracture occurs when the specimen necks down to a tiny point, as can be seen in Figure 2g. Since the sample thickness dramatically reduces after such severe plastic straining, helium bubbles become more visible, as highlighted in Figure 2h. The high resolution magnified image of the area marked by a square on the fractured NB–Cu specimen in Figure 2g, is displayed in Figure 2i. From this figure, one can observe several faceted helium bubbles embedded in the twinned Cu along with some line-like structures (marked by arrows), that possibly correspond to stacking fault debris formed during plastic deformation. Compared to the twinning stress of 0.5 GPa for the 95 nm compressive sample (See section 2.1), the 205 nm tensile specimen requires only 0.14 GPa to initiate twinning. This suggests that the twinning stress in NB–Cu samples is likely dependent on both the sample size and loading conditions.

2.3. Deformation Twin and Growth Twin Interactions

Figure 3a shows a NB–Cu pillar containing a growth twin, with its twin boundaries (TBs) oriented almost perpendicular to the loading axis. The sample is tested in tension and the tensile loading axis is along the $[7\bar{7}5]$ direction of the NB–Cu pillar. On loading, the sample yields at a stress of ≈0.75 GPa, followed by a very short stable deformation stage, as shown in the engineering stress–strain curve displayed in Figure 3k. This stage is followed by the occurrence of a sudden strain jump in the stress–strain curve that corresponds to a twin nucleating adjacent to the left TB. In Figure 3b and movie S3, this deformation twin is visible and has been marked as *T1* for reference. The CRSS for twinning in this sample was measured as ≈0.3 GPa. Since the stress required to nucleate a deformation twin in an initially 'twin-free' NB–Cu tensile sample is lower (See section 2.2), which means that presence of growth twins can strengthen the pillar. With further straining, more deformation twins get nucleated, as marked in Figure 3c as *T2* and *T3*, and are accompanied by corresponding stress drops on the stress–strain curve (see Figure 3k). As can be seen in Figure 3d, when *T3* thickens with increasing strain, a thin matrix colony starts appearing within the twin owing to variations in the local microstructure (likely containing harder helium bubbles or more dislocation debris) of the pillar. This matrix colony possibly remains untransformed because of the inhomogeneous distribution of bubbles, or bubbles with higher internal pressure, or more preexisting dislocation debris. It has been reported earlier that these factors can selectively affect the slip of dislocations.[54]

When the deformation twins start interacting with the existing growth TBs, a localized stress concentration develops in the sample. This stress concentration is identified as the bright contrast appearing near the left TB of the growth twin in Figure 3e. A massive stress drop seen in the stress–strain curves between point e and f corresponds to some internal crack nucleation and its partial propagation resulting from the local stress concentration. Also, when the crack propagates through the sample, stress relaxation occurs and the accumulated back stresses generated from dislocation-bubble interactions elicit partial detwinning of the deformation twins, as shown in Figure 3g. From Figure 3h, it can be seen that, as a result of detwinning, the matrix colony now extends up to the lower edge of the specimen. Additionally, this strain relaxation induced by crack propagation, is responsible for the formation of a small cavity/crack at the interaction point of *T2* deformation twin and growth twin boundary interface, as marked in Figure 3i. Furthermore, several large helium bubbles can be observed near the fracture surface in Figure 3j, which suggest that bubble coalescence also play a major role during the final fracture process of current growth twin embedded copper sample.[36] Although some studies[49–53] have predicted the nucleation of deformation twins within an annealing or growth twin and their interactions induced crack nucleation, our in situ experimental tests serve as the first and most compelling form of experimental evidence supporting such an internal crack nucleation mechanism.

2.4. Twinning and Detwinning in Helium Irradiated Cu under Cyclic Loading

A NB–Cu sample with width of ≈150 nm was cyclically loaded along its [$1\bar{8}2$] direction using a specially designed push to pull sample geometry in order to achieve stable in situ loading on a thin TEM foil,[55] as shown in **Figure 4**. In the first tensile loading segment, the sample shear localizes along two major slip planes, marked in Figure 4b as "twin" and "slip" (more obvious in movie S4). Due to the localized nature of twinning and slipping, two sharp surface steps can be seen at the lower edge of the sample (Figure 4b). After the first tensile loading, the deformation twin thickness is ≈16 nm. However, on reversing the load to

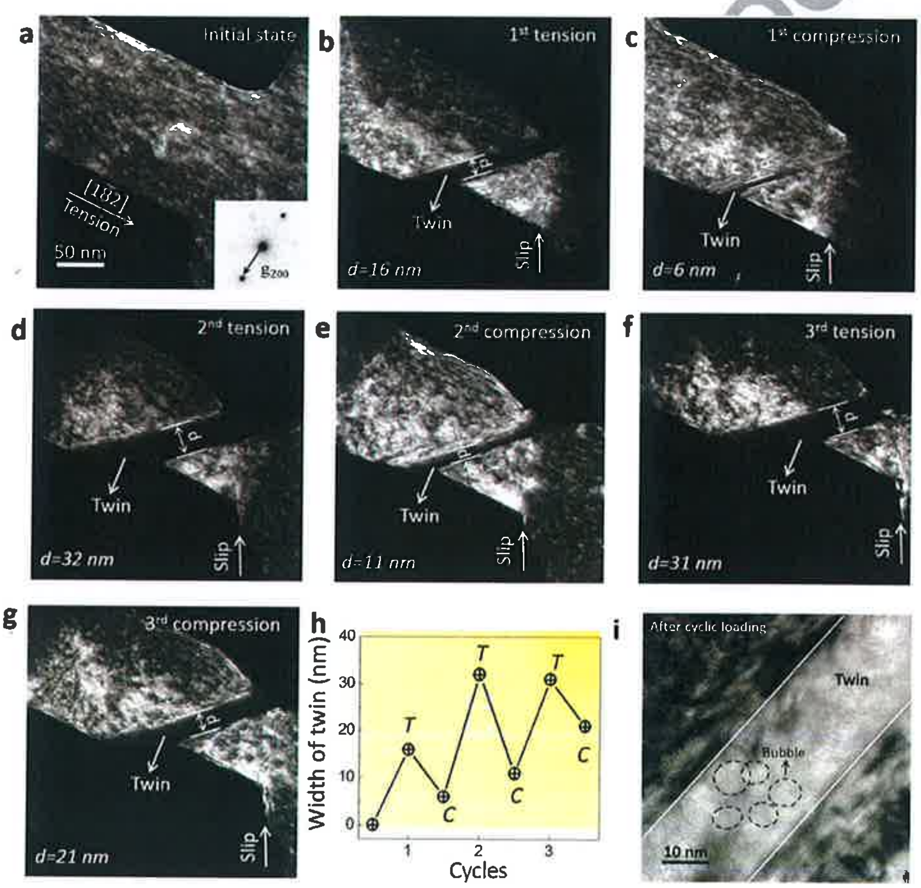

Figure 4. Cyclic loading induced twinning and detwinning of helium irradiated Cu. (a) Dark field image of the helium irradiated Cu sample with loading axis along[1]; (b) Tensile stress in the first cycle induces deformation twinning in the sample; (c) Compression in the next half of the cycle promotes detwinning and reduces the thickness of the deformation twin; (d) Second cycle of tensile deformation, increases the twin thickness compared to thickness in first tensile cycle; (e) Twin shrinks after the second cycle of compression; (f) Twin again thickens during tensile deformation; (g) After three cycles of tension-compression loading, the final thickness of the deformation twin is 21 nm; (h) Schematic illustration of the variation in the twin thickness with the cyclic loading (T and C corresponds to tension and compression, respectively); (i) Magnified image of the deformed bubbles inside the deformation twin after cyclic loading.

compression, detwinning occurs and the deformation twin width reduces to ≈6 nm, as shown in Figure 4c. This detwinning is mostly driven by the combined effect of dislocation-bubble interaction generated back stress, and partially assisted by the applied compressive stress. In the next loading cycle, tensile loading thickens the twin to 32 nm, while unloading induced detwinning and the sample shrinks it to 11 nm. The final twin thickness after successive twinning and detwinning, in the third cycle, increases to 21 nm. The progressive increase in the twin thickness during tension and compression, also illustrated by the curve in Figure 4h and movie S4, is due to the buildup of plastic strain that manifests from the inherent kinematic irreversibility of the bubble–Shockley partial dislocation interactions.

After cyclic loading, the helium bubbles distort to a more elliptical shape from their original spherical shape. To illustrate this effect, some of the distorted bubbles have been traced with dashed lines in the magnified view of the twin displayed in Figure 4i. Theoretically, since the twinning process generates a local shear strain of 0.707, the bubbles located inside the twin should deform to the elliptical shape. However, these bubbles (see Figure 4i) appear to be less deformed than what was expected. For this discrepancy, we propose that, besides twinning, plastic strain in the sample is also accommodated by dislocation slip that occurs on other slip planes intersecting the twinning plane. Therefore, dislocations cutting across bubbles from different directions evens out the shear strain introduced by twinning, and saves them from gross distortion.

2.5. Orientation and Sample Size Effect on Plasticity of Helium Irradiated Cu Pillar

In **Figure 5**a, the orientation dependence of deformation twinning and dislocation slip in submicron-sized NB–Cu and FD–Cu pillars under uniaxial loading for different crystal orientations is projected on a traditional inverse pole figure plot using the data acquired from this study (labeled by numbers) and other related reports.[36,46] It can be found that Cu single crystals that have a single slip orientation, as depicted by the blue points located in the middle of the inverse pole figure, mostly deform via full dislocation slip. Conversely, the samples with polyslip orientation, marked on lines (011)-(111) and (001)-(111), can deform either by twinning or full dislocation slip. Apart from crystal orientation, the sample size and its surface conditions also play an important role in determining the dominant deformation model. In that context, the CRSS for twinning, detwinning and slipping in NB–Cu and FD–Cu single crystals under compressive or tensile loading is plotted as a function of sample size in Figure 5b. Several interesting observations can be made and we have discussed them below. First, all NB–Cu single crystals, under both loading configurations, exhibit a much higher CRSS than the FD–Cu pillars, which indicates the obvious strengthening effect of the dense nanoscale helium bubbles formed by helium irradiation in NB–Cu pillars. The stress required to trigger twinning and detwinning is determined by the combined effect of helium bubble spacing, the stacking fault energy and the orientation of the sample. Second, the CRSS of both NB–Cu and FD–Cu submicron-sized pillars, in

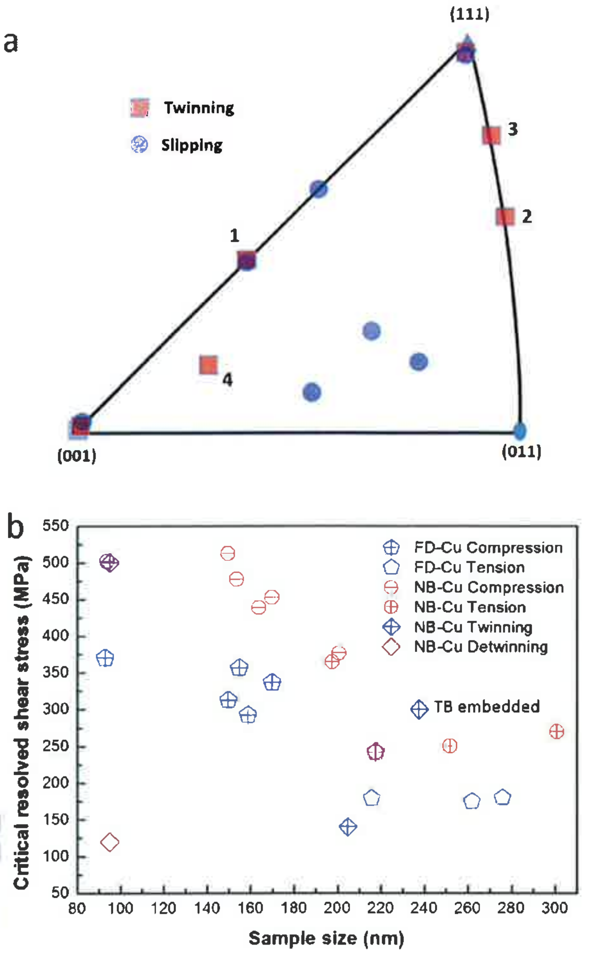

Figure 5. Orientation and sample size dependent deformation twinning and slip of submicron-sized Cu with and without nanoscale embedded helium bubbles. (a) The inverse pole figure of Cu illustrating the orientation dependence of twinning and slipping; The numbers in the triangle marked the orientations of the samples tested in Figure 1–4. (b) Variation of the critical resolved shear stress for twinning, detwinning and slipping in FD–Cu and NB–Cu as a function of sample size.

general, exhibits some size-dependence, such that smaller appears to be stronger.[55] It should be mentioned that the size effect observed in NB–Cu pillars is different from the very weak size effect observed in pillars containing shear-resistant particles[56–60] as the current NB–Cu pillar contains helium bubbles can be cut through by dislocations at elevated stresses, which could induce some extent of size-dependence as the Cu pillars containing high density of irradiation induced stacking fault tetrahedrals.[61] Third, the CRSS measured in tension is lower than that in compression for both submicron-sized NB–Cu and FD–Cu pillars, suggesting that the loading configuration/geometrical effect has a marked influence on their yield strength and plasticity. This difference in CRSS for compression and tension can be attributed to the different magnitude of normal stresses on their shear deformation planes under compression or tension.[62,63] Under compression, the normal stress on the shear plane is positive and suppresses shear deformation, whereas under tension, the normal stress on shear plane is negative and assists both slip and twinning. We can also extend this concept to explain the observed tension-compression asymmetry in the twinning stress of the pillars. Finally, owing to accumulated back stress between dislocation and bubbles interaction, detwinning occurs at a lower stress compared to twinning in submicron-sized NB–Cu samples.

3. Conclusion

By using in situ nanomechanical testing method, we found that deformation twinning and detwinning are readily activated in submicron-sized Cu pillars containing high density of nanoscale helium bubbles under uniaxial tension and compression. This process is initiated by Shockley partial dislocations, which are capable of cutting through multiple helium bubbles and assist the formation of stacking faults in the samples. With further straining, continuous partial dislocation slip occurs and leads to the nucleation of deformation twins. With the assistance of accumulated back stress, partial detwinning occurs at lower stress level when the strains are relaxed due to fracture or when the loading direction is reversed, in the NB–Cu samples. Although twinning shears the spherical bubbles to a more elliptical shape, the shape change is not exaggerated as plasticity is accommodated along other slip planes. These studies indicated that deformation twinning and detwinning are also active deformation models in helium irradiated submicron-sized copper.

Experimental Section

Sample Information: In this study, a NB–Cu sample was produced by implanting helium on an annealed, coarse-grained (average grain size 20–30 μm) Cu thin foil. To minimize the unintentional formation of other radiation defects such as dislocation loops and stacking fault tetrahedrals, the process was carried out by implanting 200 keV helium ions on Cu, with a fluence of 2×10^{17} ions cm^{-2}, at a temperature of 450 °C (high temperature promote the annihilation of dislocation loops and other single point defects etc). The sample used in current study is similar to the one used in our previous studies.[36,64] Subsequent damage and helium distribution is then estimated by performing stopping and range of ions in matter (SRIM) calculations using an average displacement energy of 29 eV for copper.[65] Additionally, the helium bubble distribution was also experimentally evaluated by imaging the cross section of a sample, prepared by the lift-out technique, inside a TEM, and is shown in Figure S1a. In this image, within the region marked by white lines, the helium concentration varies from 3 to 8 at%. From a magnified view of this region, shown in Figure S1b, the typical shape and structure of helium bubbles can be observed. Also, apart from helium bubbles, no other radiation defects were detected in the sample as expected. The average diameter of helium bubbles was measured as $\langle D \rangle \approx 6.6$ nm and their internal pressure, which does not exceed 1 GPa, was estimated based on the density and size of the helium bubbles. More details on this can be found elsewhere.[36] All the in situ mechanical tests performed on the submicron-sized Cu samples were machined from this intermediate irradiated region (marked as NB–Cu in Figure S1c) with high density of helium bubbles, as schematically illustrated in Figure S1c. The region below the helium implanted (with width of ≈760 nm from the top surface) are fully dense Cu matrix without any helium bubble and other radiation defects. The fully dense Cu pillars were cut from this part.

In situ Nanomechanical Test: In situ nanomechanical compression and tension samples were fabricated by milling this sample with a Ga-source focused ion beam (FIB, FEI Helios Nanolab 600) operated at an accelerating voltage of 30 kV, with the ion beam current not exceeding 28 pA in the final stages of polishing. In spite of exercising caution during machining, a ≈1–2 nm thick damage layer inevitably forms on the surface of some samples. The design and geometry of compressive and tensile samples employed in the tests are illustrated for reference in Figure S1d. All the pillars were cut along the normal direction and within the region marked with NB–Cu in Figure S1c and the final loading direction of the pillars were along the normal of Figure S1c, as shown in Figure S1d. To avoid surface contamination, the samples were quickly transferred to a TEM after machining. In situ mechanical tests were conducted using a Hysitron PicoIndenter (PI95) diamond tip inside a FEG JEOL 2100F TEM, which operates at an accelerating voltage of 200 kV. The displacement rates in compression and tension were programmed as 3 and 5 nm s^{-1}, respectively, to ensure that all tests were uniformly carried out at a strain rate of $\approx 10^{-3}$ s^{-1}. Prior to testing, pillars were carefully aligned with the diamond punch or tensile grip to establish uniaxial testing conditions. The whole deformation processes of the specimens during loading was recorded by a Charge-Coupled Device (CCD, Gatan 833) camera, which captured images at the rate of 10 frame per second. All the movies of in situ tests were recorded under defocused imaging conditions in order to identify the helium bubbles (with a defocus of −300 to −500 nm).

Acknowledgements

This work was supported by the National Natural Science Foundation of China (Grant Nos. 51471128, 51231005, 51621063). W.Z.H. would like to thank the support of Youth Thousand Talents Program of China, the National Key Research and Development Program of China (SQ2017YFGX090025) and the Young Talent Support Plan of XJTU. W.Z.H. acknowledges the assistance of E.G.F and Y.Q.W in ion implantation.

Supporting Information

Supporting Information is available online from the Wiley Online Library or from the author.

Conflict of Interests

xx[Q6]xx

Keywords

crack; detwinning; helium bubble; in situ TEM; twinning

Final Version: May 30, 2017
Received: April 17, 2017
Published online:

[1] M. Nastasi, J. W. Mayer, J. K. Hirvonen, *Ion-solid interactions: Fundamentals and Applications*, Cambridge University Press **1996**.[Q7]
[2] G. S. Was, *Fundamentals of Radiation Materials Science: Metals and Alloys*, Springer, Berlin Heidelberg New York **2007**.
[3] J. H. Evans, *J. Nucl. Mater.* **1977**, *68*, 129.
[4] H. Trinkaus, *Radiat. Eff. Defects Solids* **1983**, *78*, 189.
[5] S. E. Donnelly, *Radiat. Eff.* **1985**, *90*, 1.
[6] H. Trinkaus, B. N. Singh, *J. Nucl. Mater.* **2003**, *323*, 229.

[7] C. C. Fu, F. Willaime, *Phys. Rev. B* **2005**, *6*, 064117.
[8] M. J. Baldwin, R. P. Doerner, *Nucl. Fusion* **2008**, *48*, 035001.
[9] D. Brimbal, B. Decamps, J. Henry, E. Meslin, A. Barbu, *Acta Mater.* **2014**, *64*, 391.
[10] A. Caro, D. Schwen, J. Hetherly, E. Martinez, *Acta Mater.* **2015**, *89*, 14.
[11] H. Trinkaus, *J. Nucl. Mater.* **1985**, *133*, 105.
[12] B. N. Singh, H. Trinkaus, *J. Nucl. Mater.* **1992**, *186*, 153.
[13] P. Jung, J. Henry, J. Chen, J. C. Brachet, *J. Nucl. Mater.* **2003**, *318*, 241.
[14] S. J. Zinkle, G. S. Was, *Acta Mater.* **2013**, *61*, 735.
[15] W. Z. Han, N. A. Mara, Y. Q. Wang, A. Misra, M. J. Demkowicz, *J. Nucl. Mater.* **2014**, *452*, 57.
[16] T. Miura, K. Fujii, K. Fukuya, *J. Nucl. Mater.* **2015**, *457*, 279.[Q8]
[17] R. W. Siegel, S. M. Chang, R. W. Baluffi, *Acta Metall.* **1980**, *28*, 249.
[18] R. Bullough, M. R. Hayns, M. H. Wood, *J. Nucl. Mater.* **1980**, *90*, 44.
[19] S. J. Zinkle, K. Farrell, *J. Nucl. Mater.* **1989**, *168*, 262.
[20] T. D. Shen, S. Feng, M. Tang, J. A. Valdez, Y. Q. Wang, K. E. Sickafus, *Appl. Phys. Lett.* **2007**, *90*, 263115.
[21] T. Hochbauer, A. Misra, K. Hattar, R. G. Hoagland, *J. Appl. Phys.* **2005**, *98*, 123516.
[22] X. Zhang, N. Li, O. Anderoglu, H. Wang, J. G. Swadener, T. Hochbauer, A. Misra, R. G. Hoagland, *Nucl. Instrum. Methods B* **2007**, *261*, 1129.
[23] M. J. Demkowicz, A. Misra, A. Caro, *Curr. Opin. Solid State. Mater.* **2012**, *16*, 101.[Q9]
[24] W. Z. Han, M. J. Demkowicz, N. A. Mara, E. G. Fu, S. Sinha, A. D. Rollett, Y. Q. Wang, J. S. Carpenter, I. J. Beyerlein, A. Misra, *Adv. Mater.* **2013**, *25*, 6975.
[25] N. Swaminathan, P. J. Kamenski, D. Morgan, I. Szlufarska, *Acta Mater.* **2010**, *58*, 2843.
[26] W. Z. Han, E. G. Fu, M. J. Demkowicz, Y. Q. Wang, A. Misra, *J. Mater. Res.* **2013**, *28*, 2763.
[27] M. Song, Y. D. Wu, D. Chen, X. M. Wang, C. Sun, K. Y. Yu, Y. Chen, L. Shao, Y. Yang, K. T, Hartwig, X. Zhang, *Acta Mater.* **2014**, *74*, 285.
[28] C. Sun, S. Zheng, C. C. Wei, Y. Wu, L. Shao, Y. Yang, K. T. Hartwig, S. A. Maloy, S. J. Zinkle, T. R. Allen, H. Wang, X. Zhang, *Sci. Rep.* **2015**, *5*, 7801.
[29] G. R. Odette, M. J. Alinger, B. D. Wirth, *Annu. Rev. Mater. Res.* **2008**, *38*, 471.
[30] P. D. Edmondson, C. M. Parish, Y. Zhang, A. Hallen, M. K. Miller, *J. Nucl. Mater.* **2013**, *434*, 210.
[31] N. Li, N. A. Mara, Y. Wang, M. Nastasi, A. Misra, *Scr. Mater.* **2011**, *64*, 974.
[32] Q. Guo, P. L. Landau, P. Hosemann, Y. Wang, J. R. Greer, *Small* **2013**, *9*, 691.
[33] R. Liontas, X. W. Gu, E. G. Fu, Y. Q. Wang, N. Li, N. Mara, J. R. Greer, *Nano Lett.* **2014**, *14*, 5176.
[34] T. Miura, K. Fujii, K. Fukuya, *J. Nucl. Mater.* **2015**, *457*, 279.
[35] A. Reichardt, M. Ionescu, J. Davis, L. Edwards, R. P. Harrison, P. Hosemann, D. Bhatacharyya, *Acta Mater.* **2015**, *100*, 147.
[36] M. S. Ding, J. P. Du, L. Wan, S. Ogata, L. Tian, E. Ma, W. Z. Han, J. Li, Z. W. Shan, *Nano Lett.* **2016**, *16*, 4118.
[37] Z. J. Wang, F. I. Allen, Z. W. Shan, P. Hosemann, *Acta Mater.* **2016**, *121*, 78.
[38] M. A. Meyers, O. Vohringer, V. A. Lubarda, *Acta Mater.* **2001**, *49*, 4025.
[39] M. W. Chen, E. Ma, K. J. Hemker, H. W. Sheng, Y. M. Wang, X. M. Cheng, *Science* **2003**, *300*, 1275.
[40] X. Z. Liao, Y. H. Zhao, S. G. Srinivasan, Y. T. Zhu, R. Z. Valiev, D. V. Gunderov, *Appl. Phys. Lett.* **2004**, *84*, 592.
[41] K. Wang, N. R. Tao, G. Liu, J. Lu, K. Lu, *Acta Mater.* **2006**, *54*, 5281.
[42] W. Z. Han, S. D. Wu, S. X. Li, Z. F. Zhang, *Appl. Phys. Lett.* **2008**, *92*, 221909.
[43] X. L. Wu, Y. T. Zhu, *Phys. Rev. Lett.* **2008**, *101*, 025503.
[44] W. Z. Han, Z. F. Zhang, S. D. Wu, S. X. Li, *Philos. Mag.* **2008**, *88*, 3011.
[45] Y. T. Zhu, X. Z. Liao, X. L. Wu, *Prog. Mater. Sci.* **2012**, *57*, 1.
[46] Y. H. Yue, P. Liu, Q. S. Deng, E. Ma, Z. Zhang, X. D. Han, *Nano Lett.* **2012**, *12*, 4045.
[47] S. Lee, J. Lm, Y. Yoo, E. Bitzek, D. Kiener, G. Richter, B. Kim, S. H. Oh, *Nat. Commun.* **2014**, *5*, 3033.
[48] Y. Liu, J. Jian, Y. Chen, H. Wang, X. Zhang, *Appl. Phys. Lett.* **2014**, *104*, 231910.
[49] L. Lu, Y. F. Shen, X. H. Chen, L. H. Qian, K. Lu, *Science* **2004**, *304*, 422.
[50] K. Lu, L. Lu, S. Suresh, *Science* **2009**, *324*, 349.
[51] J. Wang, N. Li, O. Anderoglu, X. Zhang, A. Misra, J. Y. Huang, J. P. Hirth, *Acta Mater.* **2010**, *57*, 2262.
[52] C. J. Shute, B. D. Myers, S. Xie, T. W. Barbee, A. M. Hodge, J. R. Weertman, *Scr. Mater.* **2009**, *60*, 1073.
[53] L. L. Li, Z. J. Zhang, P. Zhang, Z. G. Wang, Z. F. Zhang, *Nat. Commun.* **2014**, *5*, 3536.
[54] Q. M. Wei, N. Li, N. Mara, M. Nastasi, A. Misra, *Acta Mater.* **2011**, *59*, 6331.
[55] M. S Ding, L. Tian, W. Z. Han, J. Li, E. Ma, Z. W. Shan, *Phys. Rev. Lett.* **2016**, *117*, 215501.
[56] J. R. Greer, J. T. M. De Hosson, *Acta Mater.* **2011**, *56*, 654.
[57] B. Girault, A. S. Schneider, C. P. Frick, E. Arzt, *Adv. Eng. Mater.* **2010**, *12*, 385.
[58] K. S. Ng, A. H. W. Ngan, *Acta Mater.* **2009**, *57*, 4902.
[59] S. H. Li, W. Z. Han, J. Li, E. Ma, Z. W. Shan, *Acta Mater.* **2016**, *126*, 202.
[60] W. Z. Han, J. Zhang, M. S. Ding, L. Lv, W. H. Wang, G. H. Wu, Z. W. Shan, J. Li, *Nano Lett.* **2017**. DOI:10.1021/acs.nanolett.7b01015.[Q10]
[61] D. Kiener, P. Hosemann, S. A. Maloy, A. M. Minor, *Nat. Mater.* **2011**, *10*, 608.
[62] Z. F. Zhang, J. Eckert, L. Schultz, *Acta Mater.* **2003**, *51*, 1167.
[63] A. C. Lund, C. A. Schuh, *Acta Mater.* **2003**, *51*, 5399.
[64] W. Z. Han, M. J. Demkowicz, E. G. Fu, Y. Q. Wang, A. Misra, *Acta Mater.* **2012**, *60*, 6341.
[65] J. F. Ziegler, J. P. Biersack, V. Littmark, *The Stopping and Range of Ions in Solids*, Pergamon, New York **1985**.

AUTHOR QUERY FORM

JOURNAL: ADVANCED ENGINEERING MATERIALS

Article: adem201700357

Dear Author,

During the copyediting of your paper, the following queries arose. Please respond to these by annotating your proofs with the necessary changes/additions using the E-annotation guidelines attached after the last page of this article.

We recommend that you provide additional clarification of answers to queries by entering your answers on the query sheet, in addition to the text mark-up.

Query No.	Query	Remark
Q1	Please confirm that given names (red) and surnames/family names (green) have been identified correctly.	
Q2	Please provide ORC ID.	
Q3	As per style of the journal, variables are set in italics. Necessary changes have been made here and elsewhere. Please check for correctness.	
Q4	Reference list and its citations have been renumbered for sequence. Please check.	
Q5	Please specify the figure number here and elsewhere.	
Q6	Please provide Conflict of Interests	
Q7	Please provide publisher location for this reference.	
Q8	Reference 16 and 34 are identical, please check and suggest.	
Q9	Please check the change made in the journal title abbreviation for this reference.	
Q10	Please provide volume and page number for this reference.	

WILEY

USING e-ANNOTATION TOOLS FOR ELECTRONIC PROOF CORRECTION

Required software to e-Annotate PDFs: Adobe Acrobat Professional or Adobe Reader (version 8.0 or above). (Note that this document uses screenshots from Adobe Reader DC.)
The latest version of Acrobat Reader can be downloaded for free at: http://get.adobe.com/reader/

Once you have Acrobat Reader open on your computer, click on the Comment tab (right-hand panel or under the Tools menu).

This will open up a ribbon panel at the top of the document. Using a tool will place a comment in the right-hand panel. The tools you will use for annotating your proof are shown below:

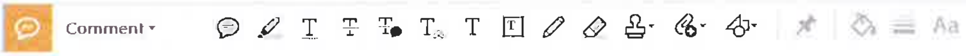

1. Replace (Ins) Tool – for replacing text.

Strikes a line through text and opens up a text box where replacement text can be entered.

How to use it:

- Highlight a word or sentence.
- Click on .
- Type the replacement text into the blue box that appears.

2. Strikethrough (Del) Tool – for deleting text.

Strikes a red line through text that is to be deleted.

How to use it:

- Highlight a word or sentence.
- Click on .
- The text will be struck out in red.

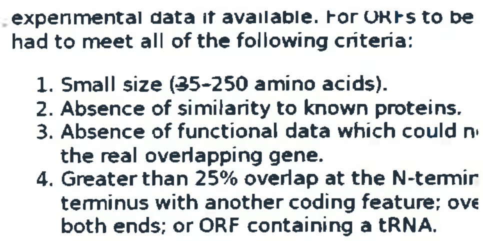

3. Commenting Tool – for highlighting a section to be changed to bold or italic or for general comments.

Use these 2 tools to highlight the text where a comment is then made.

How to use it:

- Click on .
- Click and drag over the text you need to highlight for the comment you will add.
- Click on .
- Click close to the text you just highlighted.
- Type any instructions regarding the text to be altered into the box that appears.

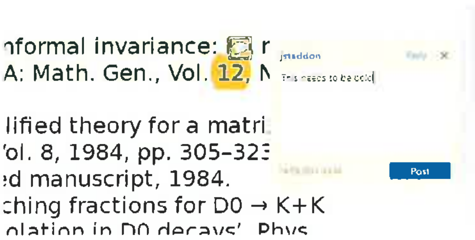

4. Insert Tool – for inserting missing text at specific points in the text.

Marks an insertion point in the text and opens up a text box where comments can be entered.

How to use it:

- Click on .
- Click at the point in the proof where the comment should be inserted.
- Type the comment into the box that appears.

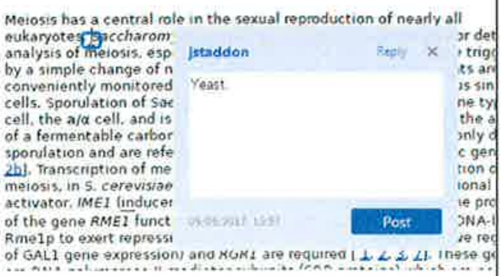

5. Attach File Tool – for inserting large amounts of text or replacement figures.

Inserts an icon linking to the attached file in the appropriate place in the text.

How to use it:

- Click on .
- Click on the proof to where you'd like the attached file to be linked.
- Select the file to be attached from your computer or network.
- Select the colour and type of icon that will appear in the proof. Click OK.

The attachment appears in the right-hand panel.

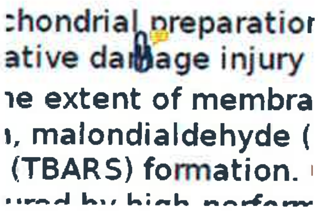

6. Add stamp Tool – for approving a proof if no corrections are required.

Inserts a selected stamp onto an appropriate place in the proof.

How to use it:

- Click on .
- Select the stamp you want to use. (The Approved stamp is usually available directly in the menu that appears. Others are shown under *Dynamic*, *Sign Here*, *Standard Business*).
- Fill in any details and then click on the proof where you'd like the stamp to appear. (Where a proof is to be approved as it is, this would normally be on the first page).

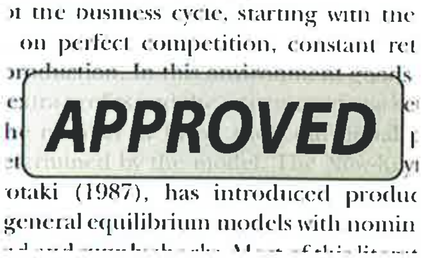

Drawing tools available on comment ribbon

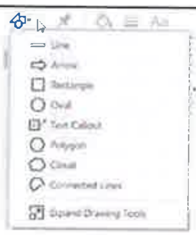

7. Drawing Markups Tools – for drawing shapes, lines, and freeform annotations on proofs and commenting on these marks.

Allows shapes, lines, and freeform annotations to be drawn on proofs and for comments to be made on these marks.

How to use it:

- Click on one of the shapes in the Drawing Markups section.
- Click on the proof at the relevant point and draw the selected shape with the cursor.
- To add a comment to the drawn shape, right-click on shape and select *Open Pop-up Note*.
- Type any text in the red box that appears.

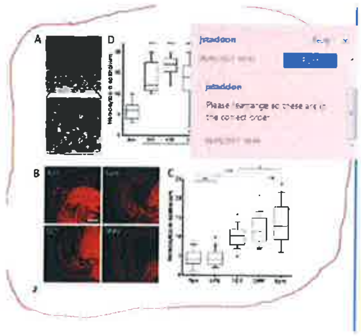

For further information on how to annotate proofs, click on the Help menu to reveal a list of further options:

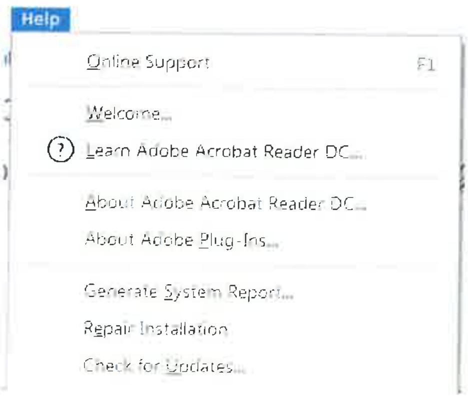

Advanced Engineering Materials

Editorial Office:
Wiley-VCH Verlag
Boschstraße 12, 69469 Weinheim
Germany

Tel.: +49 (0) 6201-606-581 or 238
Fax: +49 (0) 6201 – 606 – 510
Email: aem@wiley-vch.de

Reprint Order Form 2016

Short DOI: adem.________________

Please send me and bill me for

no. of **Reprints** via ☐ airmail (+ 25 Euro)
☐ surface mail

Please send me and bill me for a

☐ **high-resolution PDF file** (330 Euro).

My Email address:

____

Please note: It is not permitted to present the PDF file on the internet or on company homepages.

Information regarding VAT
Please note that from German sales tax point of view, the charge for **Reprints, Issues or Posters** is considered as **"supply of goods"** and therefore, in general, such delivery is a subject to German sales tax. However, this regulation has no impact on customers located outside of the European Union. Deliveries to customers outside the Community are automatically tax-exempt. Deliveries within the Community to institutional customers outside of Germany are exempted from the German tax (VAT) only if the customer provides the supplier with his/her VAT number. The VAT number (value added tax identification number) is a tax registration number used in the countries of the European Union to identify corporate entities doing business there. It starts with a country code (e.g. FR for France, GB for Great Britain) and follows by numbers.

VAT no.: ____________________
(Institutes / companies in EU countries only)

Purchase Order No.: ________________

Delivery address / Invoice address:
Name of recipient, University, Institute, Street name and Street number, Postal Code, Country

____
____
____
____
____
____
____

Date and Signature: ________________

Credit Card Payment (optional) -You will receive an invoice.

VISA, MasterCard, AMERICAN EXPRESS

Please use the Credit Card Token Generator located at the website below to create a token for secure payment. The token will be used instead of your credit card number.

Credit Card Token Generator:
https://www.wiley-vch.de/editorial_production/index.php

Please transfer your token number to the space below.

Credit Card Token Number

Price list for reprints (The prices include mailing and handling charges. All Wiley-VCH prices are exclusive of VAT)

No. of pages	Price (in Euro) for orders of					
	50 copies	100 copies	150 copies	200 copies	300 copies	500 copies
1-4	345	395	425	445	548	752
5-8	490	573	608	636	784	1077
9-12	640	739	786	824	1016	1396
13-16	780	900	958	1004	1237	1701
17-20	930	1070	1138	1196	1489	2022
for every additional 4 pages	147	169	175	188	231	315

Wiley-VCH Verlag GmbH & Co. KGaA; Location of the Company: Weinheim, Germany;
Trade Register: Mannheim, HRB 432833, Chairman of the Board: Mark Allin
General Partner: John Wiley & Sons GmbH, Location: Weinheim, Germany
Trade Register Mannheim, HRB 432296, Managing Director: Sabine Steinbach

WILEY-VCH